nanomaterials

MDPI

Article

Vanadium Carbide (V_4C_3) MXene as an Efficient Anode for Li-Ion and Na-Ion Batteries

Qiong Peng [1], Javed Rehman [2,*], Kamel Eid [3,*], Ayman S. Alofi [4], Amel Laref [5], Munirah D. Albaqami [6], Reham Ghazi Alotabi [6] and Mohamed F. Shibl [7]

1 Institution of Condensed Physics & College of Physics and Electronics Engineering, Hengyang Normal University, Hengyang 421002, China
2 Department of Physics, Balochistan University of Information Technology, Engineering and Management Sciences (BUITEMS), Quetta 87300, Baluchistan, Pakistan
3 Gas Processing Center (G.P.C.), College of Engineering, Qatar University, Doha 2713, Qatar
4 Physics Department, College of Science, Taibah University, Medina 42353, Saudi Arabia
5 Department of Physics and Astronomy, College of Science, King Saud University, Riyadh 11451, Saudi Arabia
6 Chemistry Department, College of Science, King Saud University, Riyadh 11451, Saudi Arabia
7 Center for Sustainable Development, College of Arts and Sciences, Qatar University, Doha 2713, Qatar
* Correspondence: javed.rehman@buitms.edu.pk (J.R.); kamel.eid@qu.edu.qa (K.E.)

Abstract: Li-ion batteries (LIBs) and Na-ion batteries (SIBs) are deemed green and efficient electrochemical energy storage and generation devices; meanwhile, acquiring a competent anode remains a serious challenge. Herein, the density-functional theory (DFT) was employed to investigate the performance of V_4C_3 MXene as an anode for LIBs and SIBs. The results predict the outstanding electrical conductivity when Li/Na is loaded on V_4C_3. Both $Li_{2x}V_4C_3$ and $Na_{2x}V_4C_3$ (x = 0.125, 0.5, 1, 1.5, and 2) showed expected low-average open-circuit voltages of 0.38 V and 0.14 V, respectively, along with a good Li/Na storage capacity of (223 $mAhg^{-1}$) and a good cycling performance. Furthermore, there was a low diffusion barrier of 0.048 eV for $Li_{0.0625}V_4C_3$ and 0.023 eV for $Na_{0.0625}V_4C_3$, implying the prompt intercalation/extraction of Li/Na. Based on the findings of the current study, V_4C_3-based materials may be utilized as an anode for Li/Na-ion batteries in future applications.

Keywords: V_4C_3; MXene; Li-ion battery; Na-ion battery; electrochemical energy storage; DFT

Citation: Peng, Q.; Rehman, J.; Eid, K.; Alofi, A.S.; Laref, A.; Albaqami, M.D.; Alotabi, R.G.; Shibl, M.F. Vanadium Carbide (V_4C_3) MXene as an Efficient Anode for Li-Ion and Na-Ion Batteries. *Nanomaterials* **2022**, *12*, 2825. https://doi.org/10.3390/nano12162825

Academic Editor: Robert A. Evarestov

Received: 28 May 2022
Accepted: 8 August 2022
Published: 17 August 2022

1. Introduction

The everlasting consumption of fossil fuels leads to their depletion and greenhouse gas emissions, which are the primary cause of global warming [1–3]. A variety of endeavors are currently being dedicated to addressing these issues, including gas conversion reactions [4,5] and utilizing sustainable energy sources (i.e., solar power [6,7], hydrogen power [8], fuel cells [9,10], and energy storage devices [11–15]). Li-ion batteries (LIBs) and Na-ion batteries (SIBs), with their high energy, power density, and long cycle life, are among the most beneficial electrochemical energy conversion and storage technologies available for smart grids, mobile electronics, and electric vehicles [16–18]. The performance of LIBs and SIBs is primarily shaped by the electrochemical properties of the anode materials [16,17]. Graphitic carbon is the universally utilized commercial anode material, but its low Li/Na theoretical capacity (372/25 mAh/g) and low rate capability limit its widespread, practical use [19]. Despite the significant progress in LIBs and SIBs, the earth availability of Li/Na, charge time, durability, temperature tolerance, self-discharge, and recyclability of the decayed batteries are creating a significant challenge [16–22]. Therefore, developing novel anodes with high specific capacities, greater rate capabilities, and cycling longevity is imperative.

MXenes are a novel class of 2D transition metal carbide/carbonitride electrodes that have several advantages for LIBs, SIBs, and other applications, including hydrophilicity, high active surface areas, rich electron densities, and low costs [23–25]. Numerous MXenes such as Ti_2C, Ti_3C_2, V_2C, Nb_2C, and Mo_2C were utilized as anodes for LIBs, and SIBs with

the Ti_3C_2 MXene phase has been studied most extensively [23–28]. Distinct from other MXenes, V_4C_3 MXene offers many advantages, including greater interlayer spacing, better structural durability, and high specific capacity, which are essential for the fabrication of high-performance anodes for LIBs and SIBs [29–31]. Besides its excellent mechanical properties and thermal stability, V_4C_3 MXene possesses excellent metallic properties due to its narrow band gap at the Fermi level [32,33]. Meanwhile, the vanadium metal (V) in V_4C_3 MXene has a prosperous valence state from +2 to +5, which may enhance the electrochemical performance of LIBs and SIBs [29,34,35]. For instance, the V_4C_3 MXene/MoS_2/C electrode significantly boosted LIB activity compared to MoS_2/C and MoS_2 electrodes, showing an outstanding reversible capability of 0.622 Ah/g at 1 A/g after 450 cycles and maintaining a superior rate capability of 0.5 Ah/g at 10 A/g [36]. That is due to the outstanding electrical conductivity, structural durability, and fast reaction kinetics promoted by V_4C_3. Likewise, $V_4C_3T_x$ (T = O, OH, and F), which is formed by the ball milling (B.M.) of V_4AlC_3 followed by HF etching ($V_4C_3T_x$-BM-HF), enhanced the LIB performance over $V_4C_3T_x$-HF and yielded a specific capacity of 0.225 Ah/g after 300 cycles at 0.1 A/g and 0.125 Ah/g at 1/A g because of the superior interlayer spacing and specific surface area [37]. Despite the noted progress in V_4C_3 MXene, it is rarely reported on for applications in energy storage, and usually is exclusively with regard to LIBs; to the best of our knowledge, it has not been yet addressed theoretically for both LIBs and SIBs.

In pursuit of this aim, we employed the first principle, DFT simulation, to predict the performance of V_4C_3 MXene as an anode for LIBs and SIBs as a function of Li and Na loading. V_4C_3 MXene loaded with Li/Na was investigated for lithiation, sodiation, electrical conductivity, and surface energy. The surface energy is calculated by considering Li/Na loading on V_4C_3 with a diffusion barrier of 0.023 eV for Li and 0.048 eV for Na migration.

2. Methodology

To conduct the current DFT investigations, we employed VASP software (Vienna, Austria) known as the Vienna *Ab Initio* Simulation Package [38], whereas correlation potential and the electronic exchange were examined by utilizing a generalized gradient (GGA) combined with a Perdew–Burke–Ernzerhof (PBE) functional (GGA-PBE). This is because the GGA-PBE is a nonempirical functional with judicious accuracy for qualitative and quantitative prediction of the molecules interacting and being stored with metal surfaces over a wide range of systems [39]. In the present calculations, we restricted the force value to 1/100 eV/Å, and the energy was 1×10^{-6} eV. Based on the GGA-PBE level, we simulated the electronic structure of V_4C_3 and Li/Na loaded V_4C_3. For plane-wave expansion, cut-off energy of 500 eV was selected. The Monkhorst–Pack technique was employed to sample the k-points in the Brillouin zone, with a dense k-point grid of $17 \times 17 \times 1$ [40]. Additionally, the DFT-D2 model [41] was applied in our calculations to acquire reliable binding strength between Li/Na and V_4C_3. In the structure of V_4C_3, we generated a vacuum space of 20 Å to prevent coupling between V_4C_3 layers.

Our simulations found that the materials under research are spin-polarized with Li/Na content loading. The voltage and energy profiles were computed with increasing Li/Na content, such that x = 0.125, 0.25. 0.5, 1.0, 1.5, and 2. The electronic structure calculations were carried out within the GGA-PBE to determine the electronic density of states (DOS). The AIMD simulations were used to investigate the change in the energy fluctuation of Li/Na-loaded V_4C_3 at 300 K within each time step of 1 fs for the total time duration of 5000 fs [42]. Several Li/Na concentrations were studied to procure the binding energies and voltage profile. The relationship of binding energy is shown in Equation (1) [43]:

$$E_b = \left(E_{Li-V_4C_3} + nE_{Li} - E_{V_4C_3}\right)/n, \quad (1)$$

where $E_{Li-V_4C_3}$ represents the Li-loaded V_4C_3 energy, $E_{V_4C_3}$ denotes the bare V_4C_3 energy, E_{Li} is the metallic Li energy, and n is the number of Li content loaded on the V_4C_3 sheet. Similarly, we adopt the above formula for Na adsorption by substituting Li with Na

to estimate E_b. Next, we calculate the charge density difference based on the relation: $\Delta\rho(r) = \rho_{Li-V_4C_3}(r) - \rho_{V_4C_3}(r) - \rho_{Li}(r))$. Here, $\rho_{Li-V_4C_3}$ specifies the charge density of Li-loaded V_4C_3, $\rho_{V_4C_3}$ denotes the charge density of bare V_4C_3, and ρ_{Li} is the charge density of Li (isolated). For Na-loaded V_4C_3, a similar formulation is employed by substituting only Li with Na.

For each concentration of the $Li_xV_4C_3$ compound, the open-circuit voltage (OCV) is evaluated by Equation (2) [44]:

$$V(x1,\ x2) = \left[E_{Li_{x1}} - E_{Li_{x2}} + (x_2 - x_1)\ E_{Li}\right] / (x_2 - x_1)e \quad (2)$$

where $E_{Li_{x1}}$, $E_{Li_{x2}}$, and E_{Li} are the energies of Li_{x1} V_4C_3, Li_{x2} V_4C_3, and bulk Li, respectively. A detailed discussion of the voltage profile is given in the supporting information.

The theoretical capacity (C) can be determined through Equation (3):

$$C = nF/M_{V_4C_3} \quad (3)$$

where n denotes the number of adsorbed Li/Na atoms, F defines the Faraday constant (26,801 mAh/mol), and $M_{V_4C_3}$ is the molar weight of V_4C_3.

The Bader charge technique was employed to calculate the amount of charge transferred from Li/Na to V_4C_3 (Table 1). Finally, the charging and discharging processes were investigated by using the simulation of surface barriers and minimum energy paths (MEPs) of Li/Na migration in the V_4C_3 monolayer with the climbing nudged elastic band (CI-NEB) method. This technique approximately justifies metal-ion batteries' lithiation/delithiation and sodiation/desodiation mechanisms [45].

Table 1. Structural parameters of pristine V_4C_3 MXene and Li/Na content-loaded V_4C_3 ($2 \times 2 \times 1$ supercell) at x = 0.0625, including binding energy and charge transfer.

Parameters	**Simulated Values**			
*E*ad (eV) for Li	1-site 0.90	2-site 0.884	3-site 0.828	4-site 0.897
*E*ad (eV) for Na	1.21	1.16	1.15	1.20
Charge *q* (| e |) for Li	0.84	0.83	0.83	0.883
Charge *q* (| e |) for Na	0.67	0.664	0.66	0.665
Height (h_{S-S})	6.96 Å			
Lattice constants (*a*, *b*)	2.90 Å			

3. Results and Discussion

3.1. Structure of V_4C_3 Monolayer

As a first step, we shall examine the structure of the V_4C_3 monolayer, which can be viewed in Figure 1a where the top and side views are shown. The structure portrays four layers of vanadium (V) and three layers of carbon (C) atoms. Each carbon layer is sandwiched between two V layers. In the relaxed structure, a unit-cell of V_4C_3 is composed of four V atoms and three C atoms with lattice parameters $a = b = 2.90$ Å and thickness $d = 6.96$ Å. These structural parameters are in line with the preceding results [46]. Currently, experimental data are available for the structure of V_4C_3 MXene; thus, it is interesting to investigate its anodic properties for LIBs and SIBs using DFT calculations. To determine the binding energies, the Li and Na are first adsorbed on V_4C_3 MXene. We selected four stable sites on the surface of V_4C_3 for Li/Na adsorption. The calculated E_b of the adsorbed four sites, site-1, site-2, site-3, and site-4 are 0.90 eV, 0.884 eV, 0.828 eV, and 0.897 eV, respectively, for Li (x = 0.0625). Similarly, for Na (x = 0.0625) adsorption, the binding energies are 1.21 (site-1) eV, 1.16 eV (site-2), 1.15 eV (site-3), and 1.20 eV (site-4) as depicted in Figure 1b. Comparatively, the adsorbed site-1 possesses greater binding energy for both Li/Na adsorptions. Thus, we picked site-1 for further adsorption of Li/Na loading. To avoid the repulsive interactions between $Li^+ - Li^+$ and $Na^+ - Na^+$, we consider that both surfaces (top/bottom) of V_4C_3 *MX*ene acquire reliable binding strength and maximum

Li/Na ion storage. Figure 1c depicts the decreasing binding energy curves with increasing Li/Na concentrations at $x = 2$. A decreasing trend in E_b curves is noticeable due to the $Li^+ - Li^+$ and $Na^+ - Na^+$ repulsive forces. A similar pattern was also discerned in other 2D materials upon Li/Na loading [47,48]. The various optimized Li/Na-loaded content structures with front and side views are shown in Figure 2 and Figure S1, respectively. Subsequently, we found the amount of charge transferred from Li/Na to V_4C_3 by employing the Bader charge analysis. The amount of charge transfer from Li to V_4C_3 and Na to V_4C_3 is given in Table 1 [47–49]. A large amount of charge transfer from Li/Na to V_4C_3 confirms the binding energy curve (Figure 1c). The decrease in binding energy means there is a repulsion of charge due to Coulomb forces. It could be deduced from these results that there is a charge transfer from Li/Na to the V_4C_3 surface [47–49]. This reveals that an electrochemical reaction may occur between Li/Na and V_4C_3.

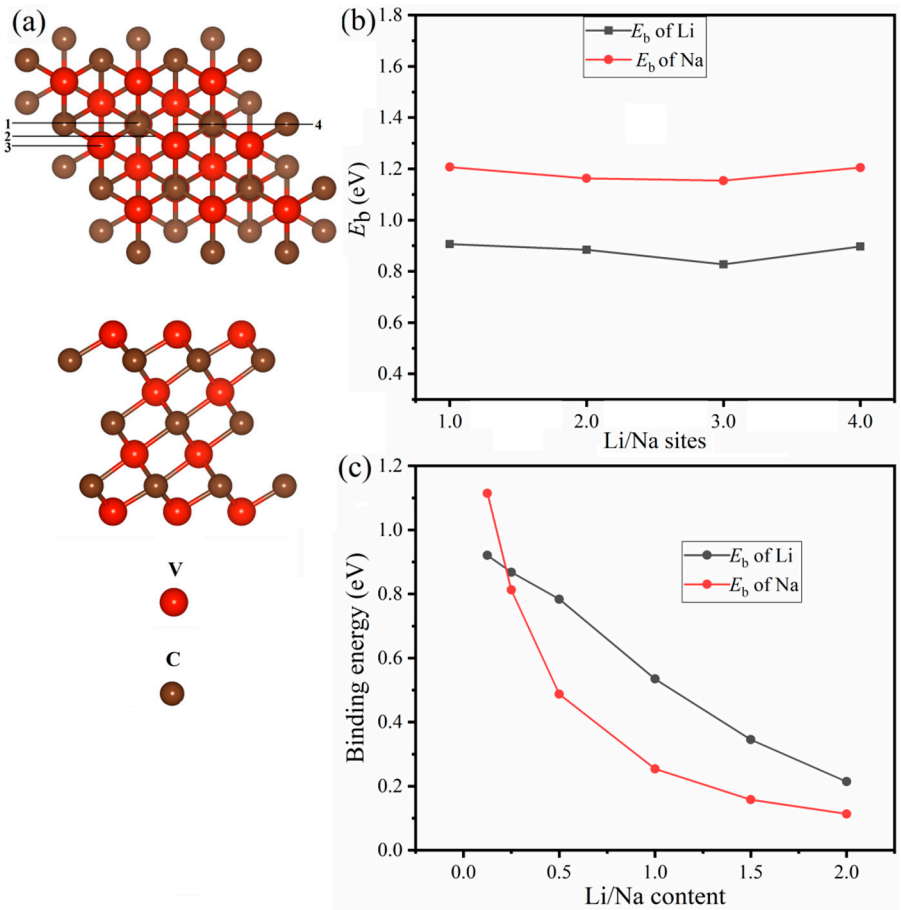

Figure 1. (**a**) Structural model of V_4C_3 *MX*ene with top and side views and (**b**) stable Li/Na sites with their E_b at $x = 0.0625$. (**c**) E_b with increasing Li/Na content. The numbers 1,2,3, and 4 represent the adsorbed four sites site-1, site-2, site-3, and site-4, respectively.

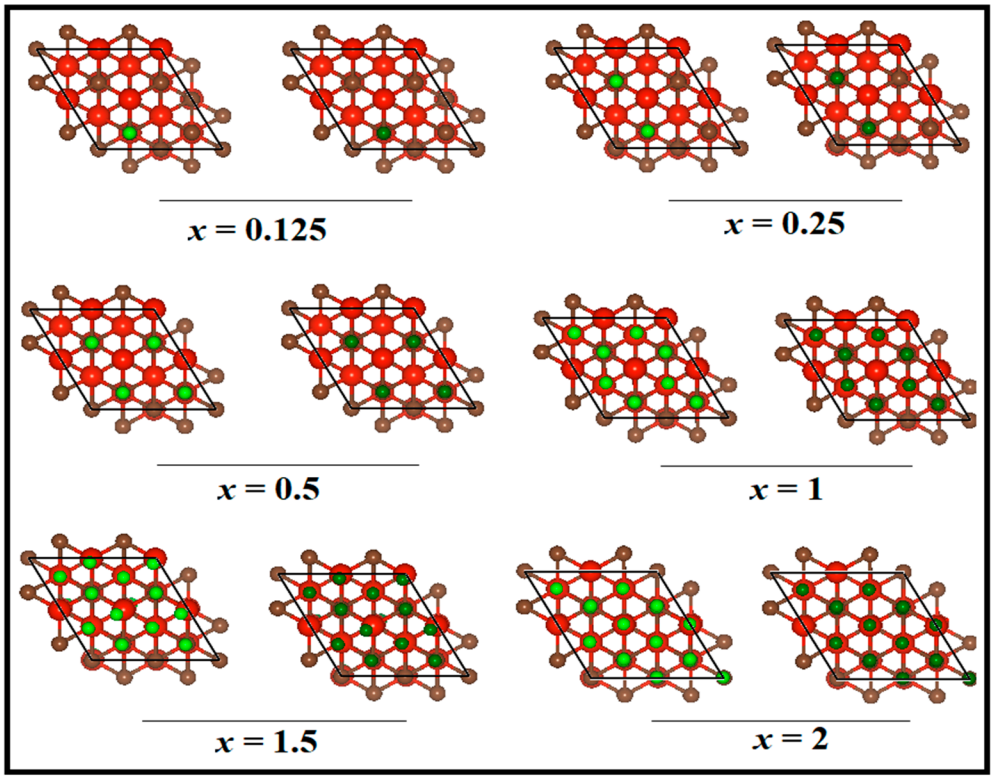

Figure 2. Front views of optimized structures of $Li_xV_4C_3$ and $Na_xV_4C_3$ at x = 0.125, 0.25, 0.5, 1, 1.5, and 2. The red color balls are V, brown ones are C, green ones are Li, and dark green ones are Na.

3.2. Safety and Stability of Li/Na-Loaded V_4C_3

Volume alteration of the V_4C_3 monolayer was studied in the in-plane expansion of the V_4C_3 single-layer (Figure S2) upon Li/Na adsorption. The results reveal that the lattice parameters increased with Li/Na adsorption increments in both $Li_{2x}V_4C_3$ and $Na_{2x}V_4C_3$, whereas the highest expected lattice expansions were about ~4.31% and 6.20%, respectively. Noticeably, V_4C_3 revealed a lower volume alteration during adsorption/desorption of Li/Na than graphite [50,51]. The energy fluctuation was computed and compared to time duration at 300 K (25 °C) using AIMD simulations to estimate the change in the structure of $Li_{2x}V_4C_3$ and $Na_{2x}V_4C_3$ (x = 0.125, 0.5, 1, 1.5, and 2) (Figure 3).

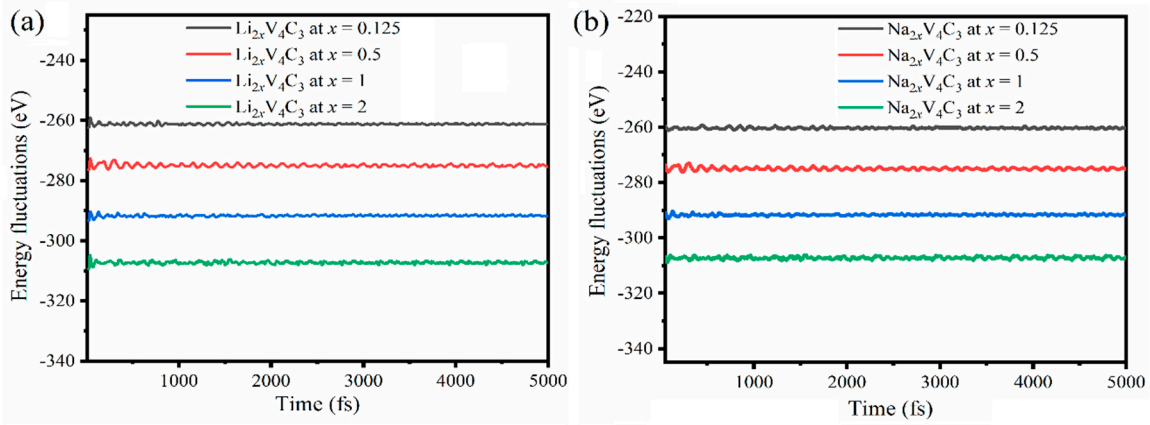

Figure 3. Energy fluctuations vs. time duration for (**a**) $Li_{2x}V_4C_3$ and (**b**) $Na_{2x}V_4C_3$ at x = 0.125, 0.5, 1, and 2.

The energy fluctuation reduced with increasing Li/Na loading in both $Li_{2x}V_4C_3$ and $Na_{2x}V_4C_3$. However, the energy remained stable without any significant change over time,

as illustrated in the straight line (Figure 3). That serves as an indication of the insignificant change in the structures of $Li_{2x}V_4C_3$ and $Na_{2x}V_4C_3$ without any deformations during Li/Na intercalation on the time scale of 1 fs to 5000 fs, which is in line with other reports on 2D materials [52–54]. We executed our simulations up to 5 ps (5000 fs) at 300 K. These steps are enough as the structure is retained at the end of 5 ps. It is noticed that the total energy converges right after as the time duration increases. Furthermore, our results show a low energy fluctuation.

3.3. Voltage and Li/Na Storage Capacity

To further examine the electrochemical behavior of V_4C_3 as a Li/Na host for LIBs and SIBs, we calculated the open-circuit voltage (OCV). Here, we discuss the anodic behavior of V_4C_3 for both LIBs and SIBs. During the lithiation and delithiation processes, the anode reaction is indicated by $V_4C_3 + xLi^+ + xe^- \rightleftarrows Li_xV_4C_3$. In this reaction, the charges (positive) start the motion between electrolyte and electrodes while the electrons pursue their motion through the external circuit of the cell. Ignoring the impact of temperature, pressure, and entropy, the voltage profile for Li/Na-loaded V_4C_3 is plotted in Figure 4a. Since the voltage profile depends on the binding energy, it decreases with the increase in Li/Na loading. However, our average voltages are estimated at around 0.38 V and 0.14 V for LIBs and SIBs. The computed voltages are underneath the described voltages of monolayers with Li/Na adsorption, where Li_xSnC is 0.44 V, $Li_xSi_2H_2$ is 0.42 V, $Na_xSi_2H_2$ is 0.64 V, Na_xSnS_2 is 1.0 V, and Na_xSnSe_2 is 0.68 V [17,55,56]. Furthermore, our evaluated average voltages also satisfy the commercial anode materials (i.e., 0.11 V for graphite and 1.5–1.8 V for TiO_2) [57,58]. Therefore, the suitable OCV designates the monolayer V_4C_3 as the superior Li/Na host material for LIBs and SIBs. Additionally, the amount of charge transfer is confirmed by evaluating the charge density difference as shown in Figure 4b,c for Li and Na, respectively. The isosurface marked with yellow exhibits the electron deficit, whilst the blue isosurface indicates the accumulated electrons. The results showed the possible charge transfer from Li/Na to the V_4C_3 surface and subsequently probable electrochemical reaction may occur between Li/Na and V_4C_3 [47–49].

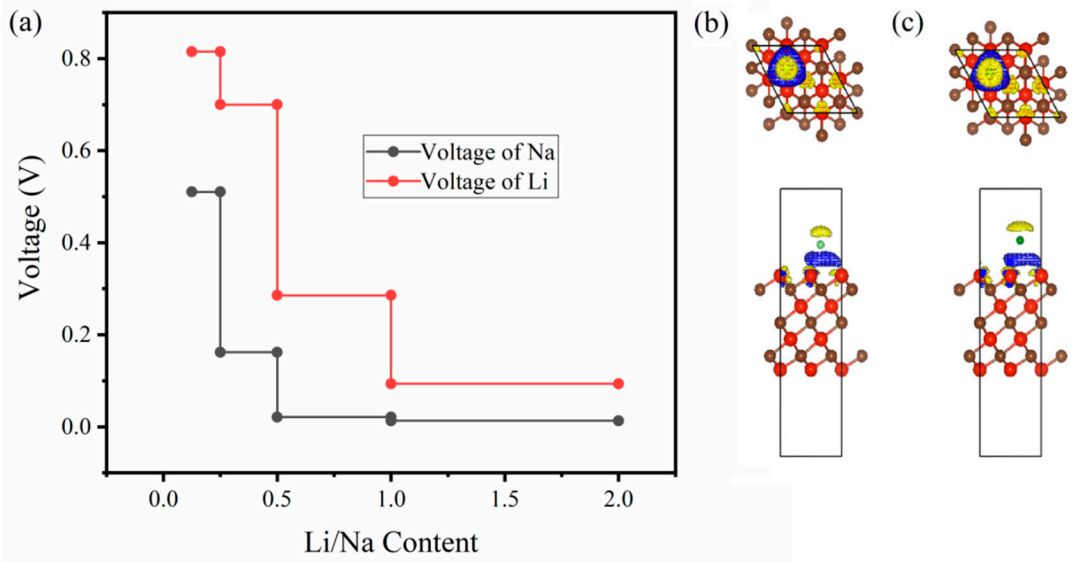

Figure 4. (**a**) Voltage plots of Li/Na. Charge density difference with front and side views of (**b**) Li adsorbed on site-1 and (**c**) Na loaded on site-1. The yellow color in (**b**,**c**) represents the electron deficit, blue is the accumulated electrons, red is V, and brown is C.

The Li/Na storage capacity of 2D V_4C_3 is computed by employing the formula [59], $C = xF/M_{V_4C_3}$. In this equation, the terms x, F, and $M_{V_4C_3}$ define the Li/Na content loaded on V_4C_3, the Faraday constant possesses a noted value of 26,801 mAh mol^{-1}, and the

molar mass is per formula unit V_4C_3, correspondingly. According to the above formula, the Li/Na storage capacity is 223.5 $mAhg^{-1}$ with a maximum loading of Li/Na content (x = 2).

3.4. Li/Na Activation Energy Barriers

In an electrochemical cell, the fast transportation of electrons and ions is desirable in a rechargeable battery to reduce the charging and discharging time. It is necessary to diffuse the metal ion at a rapid rate as it depends on the rate capability of the battery. To investigate the energy surface of V_4C_3 with Li/Na loading, we adopted a technique recognized as the climbing image nudged elastic band (CI-NEB) technique. This method is useful for finding the activation barriers and the corresponding paths. In the case of the monolayer V_4C_3 (2 × 2 × 1 supercell), we selected three minimum energy paths (MEPs), path-I (1-2-1), path-II (2-3-2), and path-III (1-4-1), for the migration of Li/Na content (x = 0.0625) as depicted in Figure 5. Five images are incorporated between the final and initial sites for each path. The simulated activation barriers for Li migration along the three pathways are 0.048 eV (path-I), 0.064 eV (path-II), and 0.073 eV (path-III). For Na migration, the computed diffusion energy barriers along the three paths are 0.048 (path-I), 0.023 eV (path-II), and 0.065 eV (path-III). The comparison of the results was made with the prior attempts, such as with Li_xMoN_2 (0.49 eV), Na_xMoN_2 (0.56 eV), Li_xVN_2 (0.237 eV), Na_xCP_3 (0.356 eV), and Li_xB_3S (0.32 eV). The MXene (V_4C_3) is dominant over other 2D materials due to its high Li/Na charging-discharging rates and low activation barriers. Moreover, we compared the diffusivity and voltages with some well-known anodes, as depicted in Table 2. The simulated results predict low diffusion energy barriers for Li/Na on V_4C_3 compared to graphitic materials (0.277~0.47 eV) [60,61], illustrating an enhanced rate capability of the host (V_4C_3) for LIBs and SIBs.

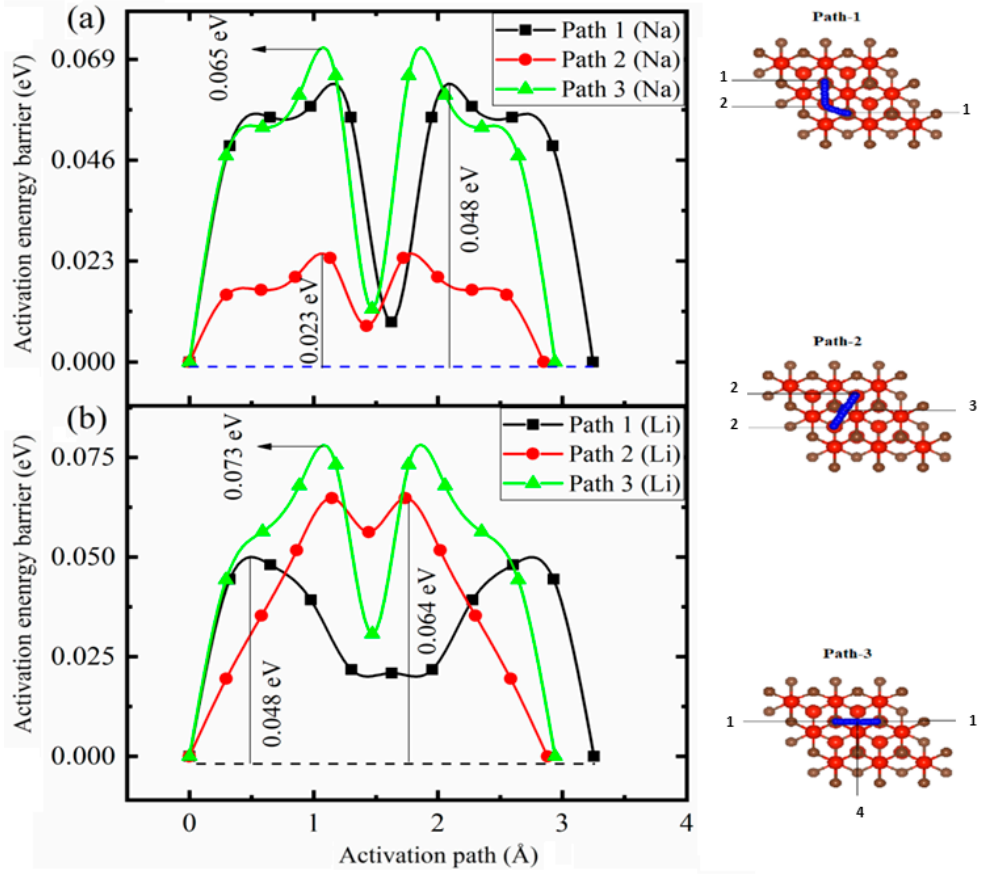

Figure 5. Activation pathways with their corresponding energy barriers of Na (**a**) and Li (**b**). The numbers (1-2-1, 2-3-2, and 1-4-1) represent the energy paths for the migration of Li/Na content (x = 0.0625).

Table 2. Comparison of voltages and energy barriers with $Li_xV_4C_3$ and $Na_xV_4C_3$.

Material	Voltage	Diffusion Barrier Energy	Method	Reference
Na_xMoS_2	0.56 V	0.08 eV	NEB	[62]
Na_xW_2C	0.43 V	0.019 eV	NEB	[59]
Na_xSiS	0.10 V	0.18 eV	CI-NEB	[63]
Li_xWSe_2	0.67 V	0.24 eV	NEB	[64]
Li_xSiH	0.42 V	0.18	CI-NEB	[56]
2D K_xPC	0.69 V	0.26 eV	NEB	[65]
2D K_xSnC	0.41 V	0.17 eV	NEB	[66]
3D Li_xPBC_2	0.48 V	0.29 eV	CI-NEB	[67]
3D Li_xSi_2BN	0.27 V	0.44 eV	NEB	[68]
$Li_xV_4C_3$	0.38 V	0.048 eV	CI-NEB	This work
$Na_xV_4C_3$	0.14 V	0.023 eV	CI-NEB	This work

3.5. Electronic Properties

Besides electronic conductivity, another essential attribute of anode materials is their superior performance. This can be assessed thoroughly to study the electronic structure, such as the density of states (DOS). Therefore, we performed the GGA-PBE calculations to establish the density of states (DOS) and partial density of states (PDOS) of pristine V_4C_3 *MX*ene and Li/Na (x = 0.0625)-loaded V_4C_3 (Figure 6). Employing the GGA-PBE technique, the DOS of the monolayer V_4C_3 was expected to be of a possible metallic nature (Figure 6a). The metallic character of the bare V_4C_3 was further examined by PDOS. The main contributions occur due to the state of V_d and C_p in the conduction band. However, the other states show small contributions to electronic conductivity. The states, such as V_p and C_s, mainly contribute to the valence band. These results justify the initial efforts made on electronic structures of the V_4C_3 [46].

The PDOS is depicted in Figure 5b,c after loading the Li/Na content on the supercell of V_4C_3 at an insignificant amount (x = 0.0625). Furthermore, the electronic structures of Li/Na-loaded V_4C_3 are inspected at x = 0.0625. At low Li/Na loading, the metallicity of the material is still maintained (i.e., Li_s or Na_s). Thus, the charge carrier transfer to the conduction band is predicted to improve electronic conductivity. The enhanced electronic conductivity suggests the better performance of V_4C_3 as an outstanding host material for both LIBs and SIBs.

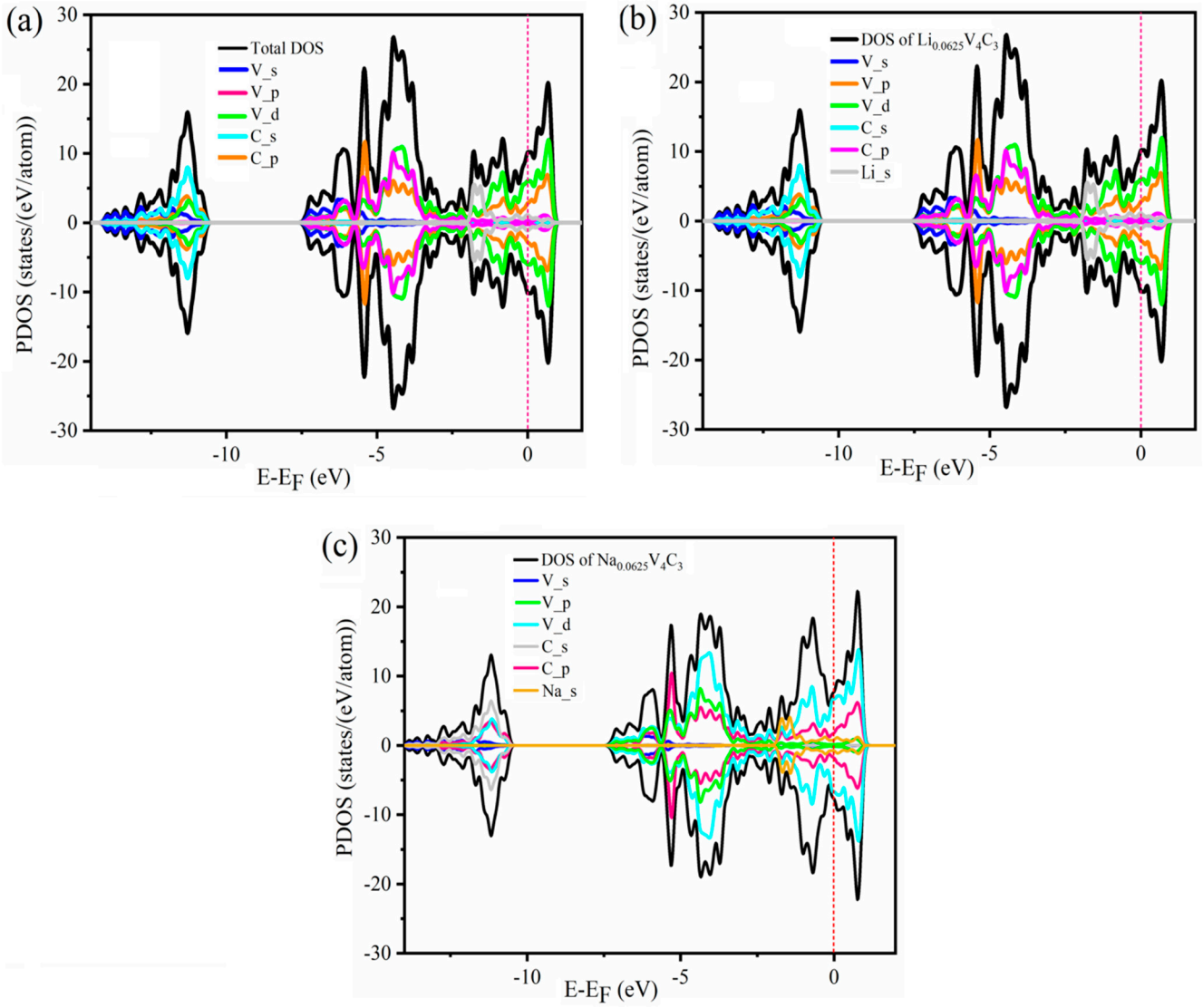

Figure 6. Density of states of (**a**) bare V_4C_3, (**b**) $Li_{0.0625}V_4C_3$, and (**c**) $Na_{0.0625}V_4C_3$.

4. Conclusions

In summary, a first-principle DFT simulation was utilized to predict the performance of V_4C_3 MXene as an anode for LIBs and SIBs. To this end, the electronic properties, durability, voltage, storage capacity, and activation barriers of Li/Na-loaded V_4C_3 were assessed. The results displayed super performances of the $Li_{2x}V_4C_3$ and $Na_{2x}V_4C_3$ as anodes for LIBs and SIBs, with an average potential of 0.38 V (for Li) and 0.14 V (for Na), as well as a reasonable Li/Na storage capacity of 223 $mAhg^{-1}$ and good cycle performance. In addition, V_4C_3 reveals very low diffusion energy barriers of 0.048 eV (for LIBs) and 0.023 eV (for SIBs), indicating the possible fast lithiation/delithiation and sodiation/desodiation processes. As the Li/Na content increased, the voltage decreased from 0.8 to 0.1 V for Li V_4C_3 and from 0.5 to 0.05 V for NaV_4C_3. During Li and Na intercalation, the energy fluctuation vs. time duration revealed a straight line, implying structural stability without any apparent deformations. The process also stems from the prompt recovery of V_4C_3, structure stability during Li/Na, and ion intercalation/extraction. The presented findings may create the opportunity for further usage of V_4C_3 as an anode material for LIBs and SIBs.

Supplementary Materials: The following supporting information can be downloaded at: https://www.mdpi.com/article/10.3390/nano12162825/s1, Figure S1: Side views of various models of Li/Na loaded on V_4C_3 monolayer, Figure S2: Variation of lattice parameters with increasing Li/Na content, and Voltage profile.

Author Contributions: All authors contributed equally to this work. Collecting the data and DFT simulation, Q.P., J.R. and M.F.S.; collecting data, A.S.A. and A.L.; writing and editing, K.E.; supervision and project administration, M.D.A. and R.G.A. All authors have read and agreed to the published version of the manuscript.

Funding: This work was financially funded by the authors express their gratitude for the support of the Researchers Supporting Project Number (RSP-2021/267) King Saud University, Riyadh, Saudi Arabia. This work is also supported by Scientific Research Fund of Hunan Provincial Education Department (No. 21B0637).

Institutional Review Board Statement: Not applicable.

Informed Consent Statement: Not applicable.

Data Availability Statement: The data presented in this study are available on request from the corresponding author.

Acknowledgments: The authors express their gratitude for the support of the Researchers Supporting Project Number (RSP-2021/267) King Saud University, Riyadh, Saudi Arabia.

Conflicts of Interest: The authors have no conflict to declare.

References

1. Lu, Q.; Eid, K.; Li, W.; Abdullah, A.M.; Xu, G.; Varma, R.S. Engineering Graphitic Carbon Nitride (g-C_3N_4) for Catalytic Reduction of CO_2 to Fuels and Chemicals: Strategy and Mechanism. *Green Chem.* **2021**, *23*, 5394–5428. [CrossRef]
2. Eid, K.; Sliem, M.H.; Eldesoky, A.S.; Al-Kandari, H.; Abdullah, A.M. Rational synthesis of one-dimensional carbon nitride-based nanofibers atomically doped with Au/Pd for efficient carbon monoxide oxidation. *Int. J. Hydrog. Energy* **2019**, *44*, 17943–17953. [CrossRef]
3. Eid, K.; Sliem, M.H.; Abdullah, A.M. Unraveling template-free fabrication of carbon nitride nanorods codoped with Pt and Pd for efficient electrochemical and photoelectrochemical carbon monoxide oxidation at room temperature. *Nanoscale* **2019**, *11*, 11755–11764. [CrossRef]
4. Eid, K.; Sliem, M.H.; Jlassi, K.; Eldesoky, A.S.; Abdo, G.G.; Al-Qaradawi, S.Y.; Sharaf, M.A.; Abdullah, A.M.; Elzatahry, A.A. Precise fabrication of porous one-dimensional gC_3N_4 nanotubes doped with Pd and Cu atoms for efficient CO oxidation and CO_2 reduction. *Inorg. Chem. Commun.* **2019**, *107*, 107460. [CrossRef]
5. Gamal, A.; Eid, K.; Abdullah, A.M. Engineering of Pt-based nanostructures for efficient dry (CO_2) reforming: Strategy and mechanism for rich-hydrogen production. *Int. J. Hydrog. Energy* **2021**, *47*, 5901–5928. [CrossRef]
6. Eid, K.; Sliem, M.H.; Abdullah, A.M. Tailoring the defects of sub-100 nm multipodal titanium nitride/oxynitride nanotubes for efficient water splitting performance. *Nanoscale Adv.* **2021**, *3*, 5016–5026. [CrossRef]
7. Eid, K.; Soliman, K.A.; Abdulmalik, D.; Mitoraj, D.; Sleim, M.H.; Liedke, M.O.; El-Sayed, H.A.; AlJaber, A.S.; Al-Qaradawi, I.Y.; Reyes, O.M. Tailored fabrication of iridium nanoparticle-sensitized titanium oxynitride nanotubes for solar-driven water splitting: Experimental insights on the photocatalytic–activity–defects relationship. *Catal. Sci. Technol.* **2020**, *10*, 801–809. [CrossRef]
8. Ahsan, M.A.; He, T.; Eid, K.; Abdullah, A.M.; Curry, M.L.; Du, A.; Puente Santiago, A.R.; Echegoyen, L.; Noveron, J.C. Tuning the intermolecular electron transfer of low-dimensional and metal-free BCN/C60 electrocatalysts via interfacial defects for efficient hydrogen and oxygen electrochemistry. *J. Am. Chem. Soc.* **2021**, *143*, 1203–1215. [CrossRef]
9. Wu, F.; Eid, K.; Abdullah, A.M.; Niu, W.; Wang, C.; Lan, Y.; Elzatahry, A.A.; Xu, G. Unveiling One-Pot Template-Free Fabrication of Exquisite Multidimensional PtNi Multicube Nanoarchitectonics for the Efficient Electrochemical Oxidation of Ethanol and Methanol with a Great Tolerance for CO. *ACS Appl. Mater. Interfaces* **2020**, *12*, 31309–31318. [CrossRef]
10. Ahsan, M.A.; He, T.; Eid, K.; Abdullah, A.M.; Sanad, M.F.; Aldalbahi, A.; Alvarado-Tenorio, B.; Du, A.; Puente Santiago, A.R.; Noveron, J.C. Controlling the Interfacial Charge Polarization of MOF-Derived 0D–2D vdW Architectures as a Unique Strategy for Bifunctional Oxygen Electrocatalysis. *ACS Appl. Mater. Interfaces* **2022**, *14*, 3919–3929. [CrossRef]
11. Song, S.H.; Park, J.S.; Song, J.H.; Lee, C.S.; Bae, J. Multi-dimensional nanocarbons hybridized with silicon oxides and their application for electrochemical capacitors. *Carbon Lett.* **2019**, *29*, 123–131. [CrossRef]
12. Rehman, J.; Eid, K.; Ali, R.; Fan, X.; Murtaza, G.; Faizan, M.; Laref, A.; Zheng, W.; Varma, R.S. Engineering of Transition Metal Sulfide Nanostructures as Efficient Electrodes for High-Performance Supercapacitors. *ACS Appl. Energy Mater.* **2022**, *6*, 6481–6498. [CrossRef]

13. Ibrahim, Y.; Mohamed, A.; Abdelgawad, A.M.; Eid, K.; Abdullah, A.M.; Elzatahry, A. The recent advances in the mechanical properties of self-standing two-dimensional MXene-based nanostructures: Deep insights into the supercapacitor. *Nanomaterials* **2020**, *10*, 1916. [CrossRef] [PubMed]
14. Chen, T.; Li, M.; Song, S.; Kim, P.; Bae, J. Biotemplate preparation of multilayered TiC nanoflakes for high performance symmetric supercapacitor. *Nano Energy* **2020**, *71*, 104549. [CrossRef]
15. Chen, T.; Bae, J. Facile One-Pot Synthesis of $LiMnO_2$ Nanowire-Graphene Nanoplatelet Composites and Their Applications in Battery-Like Electrodes for High Performance Electrochemical Capacitors. *J. Electron. Mater.* **2019**, *48*, 4240–4247. [CrossRef]
16. Rehman, J.; Fan, X.; Zheng, W. Computational insight of monolayer SnS_2 as anode material for potassium ion batteries. *Appl. Surf. Sci.* **2019**, *496*, 143625. [CrossRef]
17. Rehman, J.; Fan, X.; Butt, M.; Laref, A.; Dinh, V.A.; Zheng, W. First principles predictions of Na and K storage in layered $SnSe_2$. *Appl. Surf. Sci.* **2021**, *566*, 150522. [CrossRef]
18. Lu, Z.; Jia, C.; Yang, X.; Zhu, Y.; Sun, F.; Zhao, T.; Zhang, S.; Mao, Y. A Flexible TENG Based on Micro-Structure Film for Speed Skating Techniques Monitoring and Biomechanical Energy Harvesting. *Nanomaterials* **2022**, *12*, 1576. [CrossRef]
19. Xu, Z.L.; Park, J.; Yoon, G.; Kim, H.; Kang, K. Graphitic carbon materials for advanced sodium-ion batteries. *Small Methods* **2019**, *3*, 1800227. [CrossRef]
20. Yan, M.; Qin, Y.; Wang, L.; Song, M.; Han, D.; Jin, Q.; Zhao, S.; Zhao, M.; Li, Z.; Wang, X. Recent Advances in Biomass-Derived Carbon Materials for Sodium-Ion Energy Storage Devices. *Nanomaterials* **2022**, *12*, 930. [CrossRef]
21. Li, M.; Chen, T.; Song, S.; Li, Y.; Bae, J. HKUST-1@ IL-Li Solid-state Electrolyte with 3D Ionic Channels and Enhanced Fast Li^+ Transport for Lithium Metal Batteries at High Temperature. *Nanomaterials* **2021**, *11*, 736. [CrossRef] [PubMed]
22. Kim, P.; Chen, T.; Song, S.; Jevasuwan, W.; Lee, C.S.; Fukata, N.; Bae, J. High-capacity CVD-grown Ge nanowire anodes for lithium-ion batteries: Simple chemical etching approach for oxide removal. *J. Mater. Sci. Mater. Electron.* **2021**, *32*, 2103–2112. [CrossRef]
23. Ming, F.; Liang, H.; Huang, G.; Bayhan, Z.; Alshareef, H.N. MXenes for Rechargeable Batteries Beyond the Lithium-Ion. *Adv. Mater.* **2021**, *33*, 2004039. [CrossRef]
24. Fan, K.; Ying, Y.; Li, X.; Luo, X.; Huang, H. Theoretical investigation of V_3C_2 MXene as prospective high-capacity anode material for metal-ion (Li, Na, K, and Ca) batteries. *J. Phys. Chem. C* **2019**, *123*, 18207–18214. [CrossRef]
25. Eid, K.; Lu, Q.; Abdel-Azeim, S.; Soliman, A.; Abdullah, A.M.; Abdelgwad, A.M.; Forbes, R.P.; Ozoemena, K.I.; Varma, R.S.; Shibl, M.F. Highly exfoliated Ti_3C_2Tx MXene nanosheets atomically doped with Cu for efficient electrochemical CO_2 reduction: An experimental and theoretical study. *J. Mater. Chem. A* **2022**, *10*, 1965–1975. [CrossRef]
26. Guo, Z.; Wang, D.; Wang, Z.; Gao, Y.; Liu, J. A Free-Standing α-MoO_3/MXene Composite Anode for High-Performance Lithium Storage. *Nanomaterials* **2022**, *12*, 1422. [CrossRef]
27. Wan, K.; Li, Y.; Wang, Y.; Wei, G. Recent advance in the fabrication of 2D and 3D metal carbides-based nanomaterials for energy and environmental applications. *Nanomaterials* **2021**, *11*, 246. [CrossRef]
28. Liu, Y.; He, Y.; Vargun, E.; Plachy, T.; Saha, P.; Cheng, Q. 3D porous Ti_3C_2 MXene/NiCo-MOF composites for enhanced lithium storage. *Nanomaterials* **2020**, *10*, 695. [CrossRef]
29. Wang, X.; Li, H.; Li, H.; Lin, S.; Bai, J.; Dai, J.; Liang, C.; Zhu, X.; Sun, Y.; Dou, S. Heterostructures of Ni–Co–Al layered double hydroxide assembled on V_4C_3 MXene for high-energy hybrid supercapacitors. *J. Mater. Chem. A* **2019**, *7*, 2291–2300. [CrossRef]
30. Wang, X.; Lin, S.; Tong, H.; Huang, Y.; Tong, P.; Zhao, B.; Dai, J.; Liang, C.; Wang, H.; Zhu, X. Two-dimensional V_4C_3 MXene as high performance electrode materials for supercapacitors. *Electrochim. Acta* **2019**, *307*, 414–421. [CrossRef]
31. Wang, D.; Si, J.; Lin, S.; Zhang, R.; Huang, Y.; Yang, J.; Lu, W.; Zhu, X.; Sun, Y. Achieving Macroscopic $V_4C_3T \times$ MXene by Selectively Etching Al from V_4AlC_3 Single Crystals. *Inorg. Chem.* **2020**, *59*, 3239–3248. [CrossRef] [PubMed]
32. Chong, X.; Jiang, Y.; Zhou, R.; Feng, J. Electronic structures mechanical and thermal properties of V–C binary compounds. *RSC Adv.* **2014**, *4*, 44959–44971. [CrossRef]
33. Qin, T.; Wang, Z.; Wang, Y.; Besenbacher, F.; Otyepka, M.; Dong, M. Recent progress in emerging two-dimensional transition metal carbides. *Nano-Micro Lett.* **2021**, *13*, 183. [CrossRef]
34. Tran, M.H.; Schäfer, T.; Shahraei, A.; Dürrschnabel, M.; Molina-Luna, L.; Kramm, U.I.; Birkel, C.S. Adding a new member to the MXene family: Synthesis, structure, and electrocatalytic activity for the hydrogen evolution reaction of $V_4C_3T_x$. *ACS Appl. Energy Mater.* **2018**, *1*, 3908–3914. [CrossRef]
35. Naguib, M.; Mochalin, V.N.; Barsoum, M.W.; Gogotsi, Y. 25th anniversary article: MXenes: A new family of two-dimensional materials. *Adv. Mater.* **2014**, *26*, 992–1005. [CrossRef] [PubMed]
36. Bai, J.; Zhao, B.; Lin, S.; Li, K.; Zhou, J.; Dai, J.; Zhu, X.; Sun, Y. Construction of hierarchical V_4C_3-MXene/MoS_2/C nanohybrids for high rate lithium-ion batteries. *Nanoscale* **2020**, *12*, 1144–1154. [CrossRef]
37. Zhou, J.; Lin, S.; Huang, Y.; Tong, P.; Zhao, B.; Zhu, X.; Sun, Y. Synthesis and lithium ion storage performance of two-dimensional V_4C_3 MXene. *Chem. Eng. J.* **2019**, *373*, 203–212. [CrossRef]
38. Sun, G.; Kürti, J.; Rajczy, P.; Kertesz, M.; Hafner, J.; Kresse, G. Performance of the Vienna ab initio simulation package (VASP) in chemical applications. *J. Mol. Struct. THEOCHEM* **2003**, *624*, 37–45. [CrossRef]
39. Zhao, Y.-J.; Geng, W.; Freeman, A.; Delley, B. Structural, electronic, and magnetic properties of α-and β-MnAs: LDA and GGA investigations. *Phys. Rev. B* **2002**, *65*, 113202. [CrossRef]
40. Monkhorst, H.J.; Pack, J.D. Special points for Brillouin-zone integrations. *Phys. Rev. B* **1976**, *13*, 5188. [CrossRef]

41. Bucko, T.; Hafner, J.; Lebegue, S.; Angyan, J.G. Improved description of the structure of molecular and layered crystals: Ab initio DFT calculations with van der Waals corrections. *J. Phys. Chem. A* **2010**, *114*, 11814–11824. [CrossRef] [PubMed]
42. Van Gog, H.; Li, W.-F.; Fang, C.; Koster, R.S.; Dijkstra, M.; van Huis, M. Thermal stability and electronic and magnetic properties of atomically thin 2D transition metal oxides. *NPJ 2D Mater. Appl.* **2019**, *3*, 18. [CrossRef]
43. Tao, J.; Guan, L. Tailoring the electronic and magnetic properties of monolayer SnO by B, C, N, O and F adatoms. *Sci. Rep.* **2017**, *7*, 44568. [CrossRef] [PubMed]
44. Urban, A.; Seo, D.-H.; Ceder, G. Computational understanding of Li-ion batteries. *NPJ Comput. Mater.* **2016**, *2*, 16002. [CrossRef]
45. Henkelman, G.; Jónsson, H. Improved tangent estimate in the nudged elastic band method for finding minimum energy paths and saddle points. *J. Chem. Phys.* **2000**, *113*, 9978–9985. [CrossRef]
46. Bai, L.; Yin, H.; Zhang, X. Energy storage performance of $V_{n+1}C_n$ monolayer as electrode material studied by first-principles calculations. *RSC Adv.* **2016**, *6*, 54999–55006. [CrossRef]
47. Jena, N.K.; Araujo, R.B.; Shukla, V.; Ahuja, R. Borophane as a benchmate of graphene: A potential 2D material for anode of Li and Na-ion batteries. *ACS Appl. Mater. Interfaces* **2017**, *9*, 16148–16158. [CrossRef]
48. Xiao, B.; Li, Y.-C.; Yu, X.-F.; Cheng, J.-B. Penta-graphene: A promising anode material as the Li/Na-ion battery with both extremely high theoretical capacity and fast charge/discharge rate. *ACS Appl. Mater. Interfaces* **2016**, *8*, 35342–35352. [CrossRef]
49. Boota, M.; Jung, E.; Ahuja, R.; Hussain, T. MXene binder stabilizes pseudocapacitance of conducting polymers. *J. Mater. Chem. A* **2021**, *9*, 20356–20361. [CrossRef]
50. Vetter, J.; Novák, P.; Wagner, M.R.; Veit, C.; Möller, K.-C.; Besenhard, J.; Winter, M.; Wohlfahrt-Mehrens, M.; Vogler, C.; Hammouche, A. Ageing mechanisms in lithium-ion batteries. *J. Power Sources* **2005**, *147*, 269–281. [CrossRef]
51. Lv, X.; Li, F.; Gong, J.; Gu, J.; Lin, S.; Chen, Z. Metallic FeSe monolayer as an anode material for Li and non-Li ion batteries: A DFT study. *Phys. Chem. Chem. Phys.* **2020**, *22*, 8902–8912. [CrossRef] [PubMed]
52. Akgenc, B. New predicted two-dimensional MXenes and their structural, electronic and lattice dynamical properties. *Solid State Commun.* **2019**, *303*, 113739. [CrossRef]
53. Li, M.; Yuan, K.; Zhao, Y.; Gao, Z.; Zhao, X. A Novel Hyperbolic Two-Dimensional Carbon Material with an In-Plane Negative Poisson's Ratio Behavior and Low-Gap Semiconductor Characteristics. *ACS Omega* **2020**, *5*, 15783–15790. [CrossRef] [PubMed]
54. Lundgren, C.; Kakanakova-Georgieva, A.; Gueorguiev, G.K. A perspective on thermal stability and mechanical properties of 2D Indium Bismide from ab initio molecular dynamics. *Nanotechnology* **2022**, *33*, 335706. [CrossRef] [PubMed]
55. Rehman, J.; Fan, X.; Zheng, W. 2D SnC sheet with a small strain is a promising Li host material for Li-ion batteries. *Mater. Today Commun.* **2021**, *26*, 101768. [CrossRef]
56. Rehman, J.; Fan, X.; Samad, A.; Zheng, W. Lithiation and Sodiation of Hydrogenated Silicene: A Density Functional Theory Investigation. *ChemSusChem* **2021**, *14*, 5460–5469. [CrossRef]
57. Samad, A.; Noor-A-Alam, M.; Shin, Y.-H. First principles study of a SnS_2/graphene heterostructure: A promising anode material for rechargeable Na ion batteries. *J. Mater. Chem. A* **2016**, *4*, 14316–14323. [CrossRef]
58. Xu, S.; Fan, X.; Liu, J.; Jiang, Q.; Zheng, W.; Singh, D.J. Adsorption of Na on silicene for potential anode for Na-ion batteries. *Electrochim. Acta* **2019**, *297*, 497–503. [CrossRef]
59. Samad, A.; Shafique, A.; Kim, H.J.; Shin, Y.-H. Superionic and electronic conductivity in monolayer W_2C: Ab initio predictions. *J. Mater. Chem. A* **2017**, *5*, 11094–11099. [CrossRef]
60. Hu, J.; Liu, Y.; Liu, N.; Li, J.; Ouyang, C. Theoretical prediction of T-graphene as a promising alkali-ion battery anode offering ultrahigh capacity. *Phys. Chem. Chem. Phys.* **2020**, *22*, 3281–3289. [CrossRef]
61. Druffel, D.L.; Pawlik, J.T.; Sundberg, J.D.; McRae, L.M.; Lanetti, M.G.; Warren, S.C. First-Principles Prediction of Electrochemical Electron–Anion Exchange: Ion Insertion without Redox. *J. Phys. Chem. Lett.* **2020**, *11*, 9210–9214. [CrossRef] [PubMed]
62. Hao, J.; Zheng, J.; Ling, F.; Chen, Y.; Jing, H.; Zhou, T.; Fang, L.; Zhou, M. Strain-engineered two-dimensional MoS_2 as anode material for performance enhancement of Li/Na-ion batteries. *Sci. Rep.* **2018**, *8*, 2079. [CrossRef] [PubMed]
63. Pham, T.D.; Luong, H.D.; Sato, K.; Shibutani, Y.; Dinh, V.A. Two-dimensional Na_xSiS as a promising anode material for rechargeable sodium-based batteries: Ab initio material design. *Phys. Chem. Chem. Phys.* **2019**, *21*, 24326–24332. [CrossRef]
64. Rehman, J.; Ali, R.; Ahmad, N.; Lv, X.; Guo, C. Theoretical investigation of strain-engineered WSe_2 monolayers as anode material for Li-ion batteries. *J. Alloy. Compd.* **2019**, *804*, 370–375. [CrossRef]
65. Dou, K.; Ma, Y.; Zhang, T.; Huang, B.; Dai, Y. Prediction of two-dimensional PC_6 as a promising anode material for potassium-ion batteries. *Phys. Chem. Chem. Phys.* **2019**, *21*, 26212–26218. [CrossRef] [PubMed]
66. Rehman, J.; Fan, X.; Laref, A.; Zheng, W. Adsorption and Diffusion of Potassium on 2D SnC Sheets for Potential High-Performance Anodic Applications of Potassium-Ion Batteries. *ChemElectroChem* **2020**, *7*, 3832–3838. [CrossRef]
67. Younis, U.; Muhammad, I.; Qayyum, F.; Kawazoe, Y.; Sun, Q. A stable metallic 3D porous BPC_2 as a universal anode material for Li, Na, and K ion batteries with high performance. *J. Mater. Chem. A* **2020**, *8*, 25824–25830. [CrossRef]
68. Younis, U.; Muhammad, I.; Wu, W.; Ahmed, S.; Sun, Q.; Jena, P. Assembling Si_2BN nanoribbons into a 3D porous structure as a universal anode material for both Li-and Na-ion batteries with high performance. *Nanoscale* **2020**, *12*, 19367–19374. [CrossRef]